WILEY

RESEARCH ARTICLE

Near-Field Microwave Holographic Imaging Using a Metamaterial-Based Diffraction Neural Network With Angular Spectrum-Assisted Computation

Ying Li[1] (iD) | Li Deng[1] (iD) | Meijun Qu[2] (iD)

[1]School of Information and Communication Engineering, Beijing University of Posts and Telecommunications, Beijing, Beijing, China | [2]State Key Laboratory of Media Convergence and Communication, School of Information and Communication Engineering, Communication University of China, Beijing, Beijing, China

Correspondence: Li Deng (dengl@bupt.edu.cn)

ABSTRACT

This Letter focuses on the imaging capability of a diffraction neural network. By combining the Rayleigh–Sommerfeld diffraction equation with neural network connectivity rules, we design a diffraction neural network model for holographic imaging on a zero-information input plane. The model is implemented using the angular spectrum method and fast Fourier transform algorithm. Training is performed via error backpropagation and a stochastic gradient descent algorithm. We analyze the theoretical influence of key network parameters and conduct simulation-based studies to explore the effects of unit size, working wavelength, and diffraction propagation distance on imaging performance. Metamaterials are used to simulate Huygens diffraction neurons. A physical-layer model of the diffraction neural network is constructed using metamaterial parameter mapping, and its effectiveness is evaluated through full-wave electromagnetic simulations. The simulation results demonstrate the feasibility and potential of the proposed imaging system based on the diffraction neural network.

1 | Introduction

Microwave holographic imaging (MHI) employs electromagnetic radiation within the microwave spectrum and holds significant application value in security, remote sensing, detection, and medical diagnosis [1–4]. Serving as an extension of optical holography, MHI assumes a vital role in holographic technology research due to its extended wavelength and impressive penetration capabilities. Conventional interferometry holography necessitates intricate recording media and reconstruction methods and Initial microwave holography relied on synthetic aperture radar (SAR) [5], demanding multiple transceiver antennas and ultra-wideband pulses, resulting in complexity. As computational technology advanced, the concept of utilizing computers

for hologram generation garnered attention [6–8]. Through mathematical description and simulation calculation of the wavefront information of electromagnetic scattering of objects to generate holograms, and then use special media such as metamaterials to restore image information. which is called Computer-generated hologram (CGH). This technique generates images not constrained by reality and liberates reliance on recording media. In 1971, Gerchberg and Saxton proposed the GS algorithm using Fourier transform and inverse Fourier transform iteration to recover phase information [9], which pioneered the CGH algorithm.

Artificial intelligence (AI) is also being explored for tackling electromagnetic imaging challenges. Psaltis introduced neural

---

networks for hologram generation [10], while Rekanos suggested radial basis function neural networks (RBFNN) to address inverse scattering issues in microwave imaging [11]. Additional techniques like support vector machine (SVM) and support vector regression (SVR) have been experimented with [12–14]. However, the outcomes of these endeavors have been relatively unsatisfactory due to the limitations of conventional neural network technology. Yet, as artificial intelligence technology evolves, deep learning techniques, which have found success in the realm of computer vision, have demonstrated their potential for electromagnetic imaging. Notably, it can significantly improve the imaging speed and quality [15]. Built upon the concept of physically-assisted learning, incorporating domain expertise into neural networks effectively alleviates the learning burden on deep neural networks and prevents them from redundantly learning well-established Maxwell's equations. Lin Xing et al. introduced the Diffraction deep neural network (D^2NN) in 2018 [16]. Based on the simple Huygens principle, this approach amalgamates diffraction theory calculations with deep learning techniques to create an simple artificial intelligence entity grounded in electromagnetic wave interactions. The diffraction neural network (DNN) achieves precise control over electromagnetic wave near-fields, offering promising potential for high-precision imaging. In Ref. [17], a method for generating THz-band holograms based on DNN is proposed. Experimental results showcase excellent fitting performance of DNN within the near-optical band, coupled with swift computational speed. However, due to the high-frequency nature of the THz band, optimal imaging planes exhibit substantial distance offsets, demanding considerable hardware resources for training algorithms. This aspect hampers the feasibility of portable applications.

In this letter, a DNN-based holographic imaging algorithm in the microwave frequency band is proposed and evaluated as shown in Figure 1. The FFT algorithm is employed to accelerate the computation of the phase distribution required for target imaging, enabling faster processing without the need for GPU acceleration. The feasibility of the algorithm is demonstrated through metamaterial-based phase mapping and verified via full-wave electromagnetic simulations at 30 GHz. Although a 3D-printed hologram prototype was designed for future experimental validation, the current results are obtained from
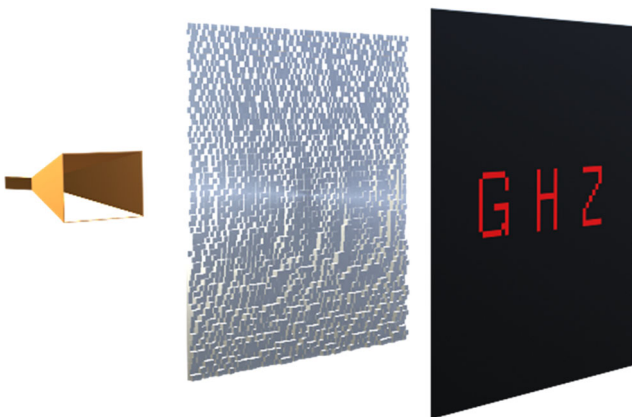

FIGURE 1 | Microwave holographic imaging structure based on DNN.

simulation. These simulation results confirm that the holograms generated by the DNN possess the capability to accurately reconstruct the target image.

2 | Methods

The imaging system employs a holographic approach facilitated by the DNN algorithm. The neural network model is established through forward propagation, while the requisite phase surface for imaging is honed via back propagation. The methodology for constructing this model is detailed as follows. Drawing upon the Rayleigh-Sommerfeld diffraction theory and the angular spectrum method, and guided by the Huygens principle, each unit within the diffraction layer emits a modulated wavelet, effectively functioning as a secondary wave source. This conceptualization permits the interpretation of the spatial propagation processes amid the diffraction layers as a comprehensive, fully connected neural network. Consequently, the holographic phase surface is analogous to a concealed layer housing trainable variables within this framework.

2.1 | Forward Propagation

As illustrated in Figure 2, the process of forward propagation within the DNN aligns with the simulated propagation of electromagnetic waves. As these waves traverse the diffraction layer, the phase modulation induced by the layer can be mathematically represented as $U_1(x_i, y_i, z_i) = U_0(x_i, y_i, z_i) \cdot \alpha_i e^{j\varphi_i}$. Here, φ_i corresponds to the phase response at the specific location (x_i, y_i, z_i) on the diffraction layer, while α_i signifies the amplitude response at the same position. The complex vector of the wave is denoted as $U(x, y, z)$.

In the context of approximating the electromagnetic wave as a scalar, it is assumed that the electric field is relatively decoupled from the magnetic field, thus disregarding the vector properties of the electromagnetic field. Drawing on the Rayleigh-Sommerfeld diffraction theory, the computation of the diffraction field within space can be treated as a convolution operation involving the incident field and the spatial impulse response:

$$U_2(x, y, z) = h(x, y, z) * U_1(x_i, y_i, z_i) \tag{1}$$

and

$$h(x, y, z) = \frac{1}{2\pi} \frac{z - z_i}{r} \left(\frac{1}{r} - jk \right) \frac{e^{jkr}}{r} \tag{2}$$

where $r = \sqrt{(x - x_i)^2 + (y - y_i)^2 + (z - z_i)^2}$. Applying the angular spectrum theory, one can derive the spatial transfer function as follows:

$$H(f_x, f_y) = \mathcal{F}\{h(x, y)\} = e^{j2\pi z \sqrt{\lambda^2 - (f_x)^2 - (f_y)^2}} \tag{3}$$

where $\mathcal{F}\{\cdot\}$ represents the Fourier transform operation, and f_x and f_y denote the spatial frequencies in the x and y directions, respectively. The numerical computation of this transformation can be efficiently executed using the Fast Fourier Transform
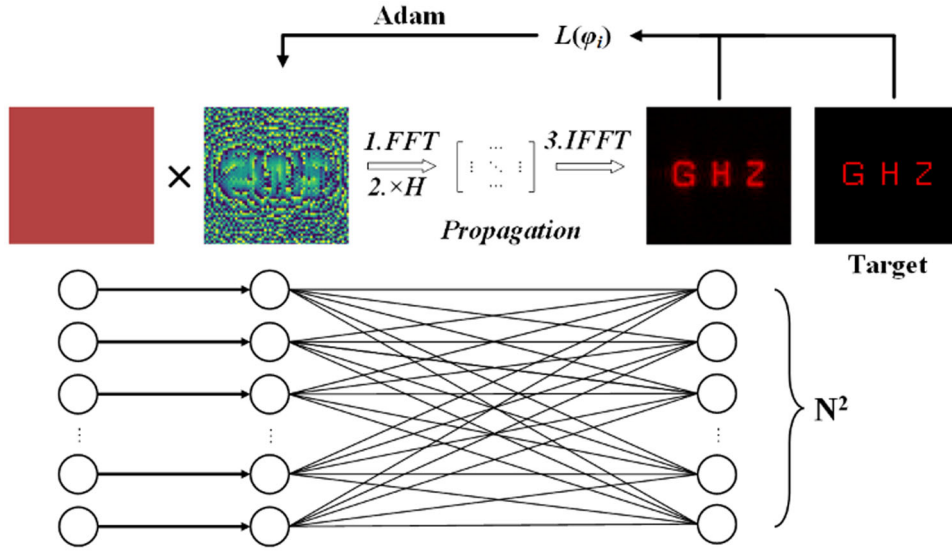
FIGURE 2 | The schematic diagram of microwave holographic imaging algorithm based on DNN.

(FFT) algorithm, enabling swift calculation of the diffraction field distribution. As a result, the forward propagation process of neurons within the DNN can be defined as the subsequent diffraction propagation process:

$$f_{out} = \mathcal{F}^{-1}\{\mathcal{F}\{f_{in} \cdot \alpha_i e^{j\varphi_i} \cdot H(f_x, f_y)\}\} \tag{4}$$

where f_{out} represents the output of the network, and f_{in} corresponds to the input of the network. In the context of the imaging system, the ultimate output field manifests as the amplitude of the imaging plane: $I_{out} = |f_{out}|$.

2.2 | Loss Function and Back Propagation

To appraise the effectiveness of microwave imaging through DNN, it becomes imperative to establish the error loss function between the intensity of the output field and the intended target. In the context of DNN imaging, viewing the network as a function of two-dimensional values within an independent variable, the imaging endeavor can be likened to a linear regression scenario. Consequently, the DNN employs a modified mean squared error loss (MMSE) as its chosen loss function:

$$L(\varphi_i) = \frac{1}{K} \sum_{K=1}^{K} \left(\frac{|f_{out}|^2}{\sum |f_{out}|^2} - \frac{|T_K|^2}{\sum |T_K|^2} \right)^2 \tag{5}$$

where i is the ith diffracting neuron, l is the lth diffracting layer, K is the total number of imaging points in the imaging plane, and k is the kth imaging point in the imaging plane. T_k represents the kth pixel value of the target image matrix $\boldsymbol{T}$.

This can be explained by the fact that the difference between the calculated amplitude value and the set target image value is too large to be applied to the direct calculation of the amplitude difference. Therefore, to improve the imaging quality, it is

necessary to improve the light and dark contrast of the imaging area. However, the amplitude difference of the target image is fixed, so the amplitude difference is changed to the difference between the proportion of the sum of the energy of the imaging point in the whole imaging surface and the proportion of the sum of the energy of the pixels in the target image in the whole image surface. When only phase variables are trained, the optimization problem can be described as:

$$\min_{\varphi_i \in [0, 2\pi]} L(\varphi_i) \tag{6}$$

The Adaptive Moment Estimation (Adam) method is used to propagate the error back and update the DNN network parameters. When calculating the gradient, it is found that the gradient law of the output field to the phase is as follows:

$$\begin{aligned} \frac{\partial f_{out}}{\partial \varphi_i} &= \frac{\partial [\mathcal{F}^{-1}\{\mathcal{F}\{f_{in} \cdot \alpha_i e^{j\varphi_i}\} \cdot H(f_x, f_y)\}]}{\partial \varphi_i} \\ &= \frac{\mathcal{F}^{-1}\{\mathcal{F}\{f_{in} \cdot \alpha_i \cdot \partial [e^{j\varphi_i}]\} \cdot H(f_x, f_y)\}}{\partial \varphi_i} = j \cdot f_{out} \end{aligned} \tag{7}$$
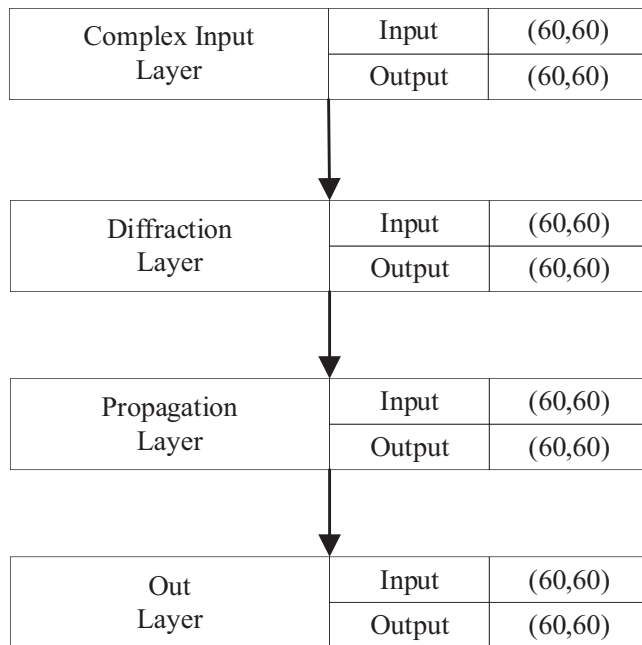
The fast Fourier transform calculation of the matrix is independent of the phase for the frequency domain and the spatial domain, so the calculation of the partial derivative can be exchanged with the FFT calculation order. Since the gradient representation of the loss function, the only variable is the partial derivative of the output plane to the phase variable. This law provides convenience for gradient descent calculation.

2.3 | Training Results and Parametric Analysis

To verify the feasibility of the microwave imaging system based on DNN, the target image of 60×60 pixels and the network of the same size are set. The DNN design parameters are shown in Table 1. In the Windows system, TensorFlow (v2.9.0, Google Inc.), one of the deep learning frameworks developed by

TABLE 1 | DNN design parameters.

Parameter name	Value
Size	60*60
Layer number	1 layer
Learning rate	0.05
Epoch	1000
Cell size(L_N)	5 (mm)
Lambda(λ_c)	10 (mm)
Frequency(f_c)	30 (GHz)
Propagation distance(Z_c)	100 (mm)

Complex Input Layer	Input	(60,60)
	Output	(60,60)

Diffraction Layer	Input	(60,60)
	Output	(60,60)

Propagation Layer	Input	(60,60)
	Output	(60,60)

Out Layer	Input	(60,60)
	Output	(60,60)

FIGURE 3 | DNN imaging task data flow diagram.

Google, is used to program with Python (v3.8.0) language. The target image matrix T is input into the DNN model, and the data flow diagram shown in Figure 3 is obtained.

In the training process, taking $\alpha_i = |S_{21}(\varphi_i)|$, and S_{21} is the transmission coefficient of the dielectric column, which can make the calculation result more accurate. The target image and the calculated imaging result are shown in Figure 4a,b. Using the MMSE loss function, the amplitude peak of the image becomes 3.76 times of the original, and the excess energy is collected from the surrounding dark area to the imaging point. Figure 4c shows the phase distribution obtained by training 1000 epoch. The contour state of one circle proves the principle of DNN focusing imaging. Figure 4d shows the curve of the loss function decreasing with the training epoch, indicating that the algorithm has a very fast convergence speed, even in the absence of graphics processing unit (GPU) hardware acceleration.

Among the parameters of DNN, the most influential is the ratio of central working wavelength λ_c to cell size L_N. Figure 5 shows

the training imaging results of $L_N = 0.1\lambda_c \sim 1.0\lambda_c$. Due to the inherent principle of RS theory, in the process of discretizing space into diffractive neurons according to Huygens principle, the spatial domain is actually sampled. When FFT is used for calculation, the frequency domain is actually sampled. Therefore, according to the Nyquist sampling condition: $f_s > 2f_m$ needs to be satisfied. Otherwise, the spatial or frequency domain aliasing will occur, resulting in the distortion noise of imaging cannot be eliminated by gradient descent, Therefore, the central working wavelength λ_c and cell size L_N need to satisfy:

$$L_N \geq 0.5\lambda_c \tag{8}$$

However, the energy of the diffraction unit is mainly concentrated in the aperture, and the maximum half-cone diffraction angle is $\varphi_{max} = \sin^{-1}(\frac{\lambda}{2L_N})$. So the diffraction beam is concentrated in the main lobe area ($\sqrt{x^2 + y^2} \leq z \tan\varphi_{max}$) to meet the requirements of the fully connected network. Otherwise, the energy cannot be concentrated, and the trained image has stripe distortion. The central working wavelength λ_c and cell size L_N also need to satisfy:

$$N^2 L_N^2 \left(\frac{4L_N^2}{\lambda_c} - 1 \right) \leq Z_c^2 \tag{9}$$

It can be observed that the upper limit of Cell size L_N is related to the diffraction propagation distance Z_c. The larger Z_c is, the looser the upper limit of L_N is. However, due to the attenuation of electromagnetic wave propagation in the air, the propagation distance needs to be kept in a reasonable range. For the diffraction wave, the propagation distance $Z_c = 100mm$ is set by training, and the theoretical loss is about 40 dB.

Under the limitation of these three conditions, $L_N = 0.5\lambda_c$ is the best. For other parameters, the training results show that the training process has little effect within a reasonable range, and will not shown here for clarity.

3 | Imaging Simulation Based on Metamaterial Unit

After the DNN training is completed, the physical entity of the DNN will be realized. The metamaterial unit is used to simulate the Huygens-Fresnel diffraction neuron to apply a phase factor to the input field, and then the phase distribution is converted into a metamaterial parameter distribution that can be linearly adjusted. After the modeling is completed, the simulation results are observed in the electromagnetic field solver.

The unit structure as simple as possible is not only convenient for theoretical calculation, but also reduces the difficulty of simulation. To control the phase of electromagnetic wave simply, a regular square unit structure shown in the subgraph of Figure 6 is considered. The vertical incident electromagnetic wave depends on the phase accumulation gradually with distance inside the material unit to achieve the purpose of
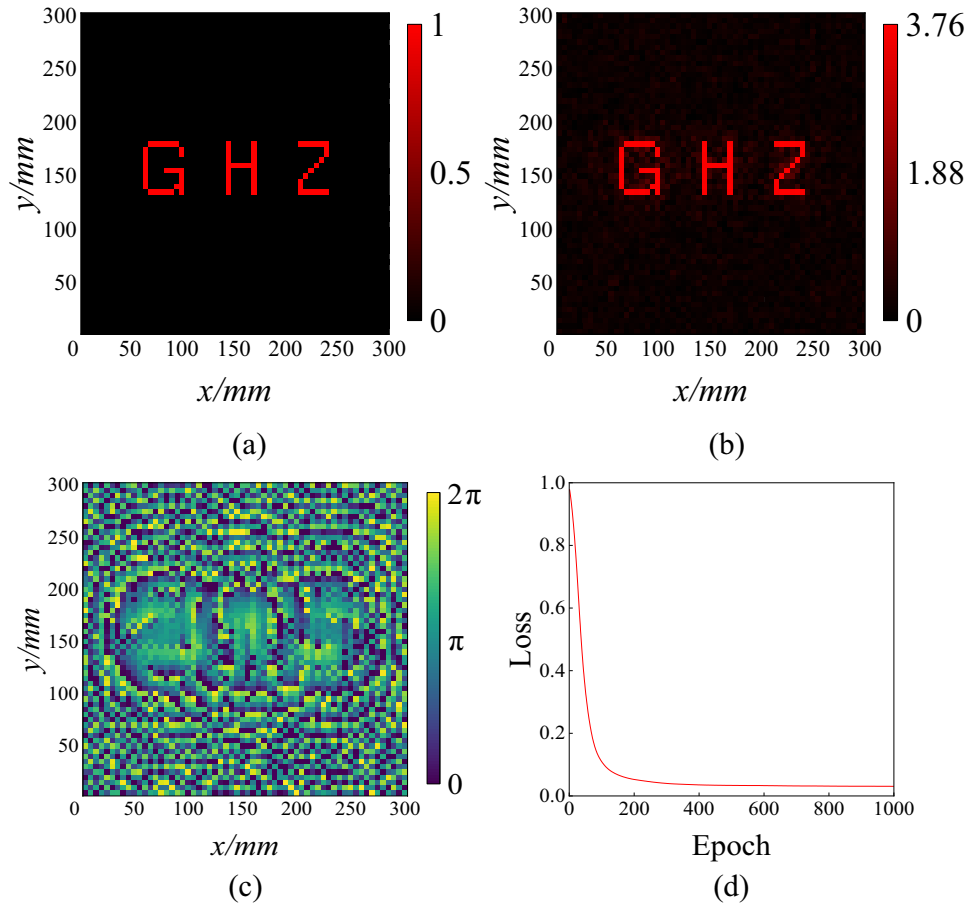
FIGURE 4 | (a) Target intensity profile. (b) Calculated result of image training. (c) Phase distribution maps. (d) Training loss versus epoch.
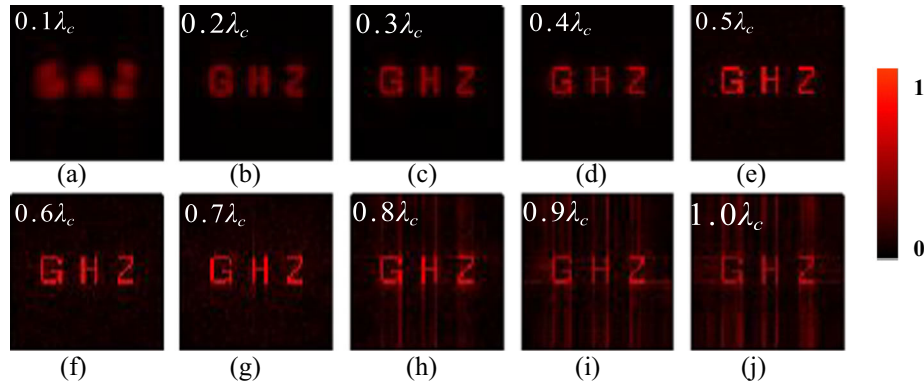

FIGURE 5 | (a–j) Imaging result by DNN training about $L_N = 0.1\lambda_c \sim 1.0\lambda_c$.

controlling the phase of the exit. The unit structure is as follows, the unit side length is L_N, and the unit height is h.

According to the transmission line theory, the theoretical results of the transmission coefficient of the unit can be calculated:

$$S_{21} = \frac{(1 - \Gamma^2)e^{-j\beta h}}{1 - \Gamma^2 e^{-2j\beta h}} \tag{10}$$

where $\beta = 2\pi f_c \sqrt{\mu_r \varepsilon_r}$ is the propagation constant of the wave inside the unit, and Γ is the reflection coefficient of the unit, which is expressed as follows:

$$\Gamma = \frac{\sqrt{\mu_r / \varepsilon_r} - 1}{\sqrt{\mu_r / \varepsilon_r} + 1} \tag{11}$$

For the material with good transmittance, due to the low reflection coefficient, the real part of the denominator in Formula (10) is close to 1, and the imaginary part is close to 0. The phase response of S_{21} with height h is very close to linear, and the theoretical slope is about $-\beta$. Using High Frequency Structure Simulator (HFSS19.2) simulation solution, the Master-Slave boundary conditions and Floquet port excitation are set, and the dielectric material is set to be the commonly used rigid opaque white
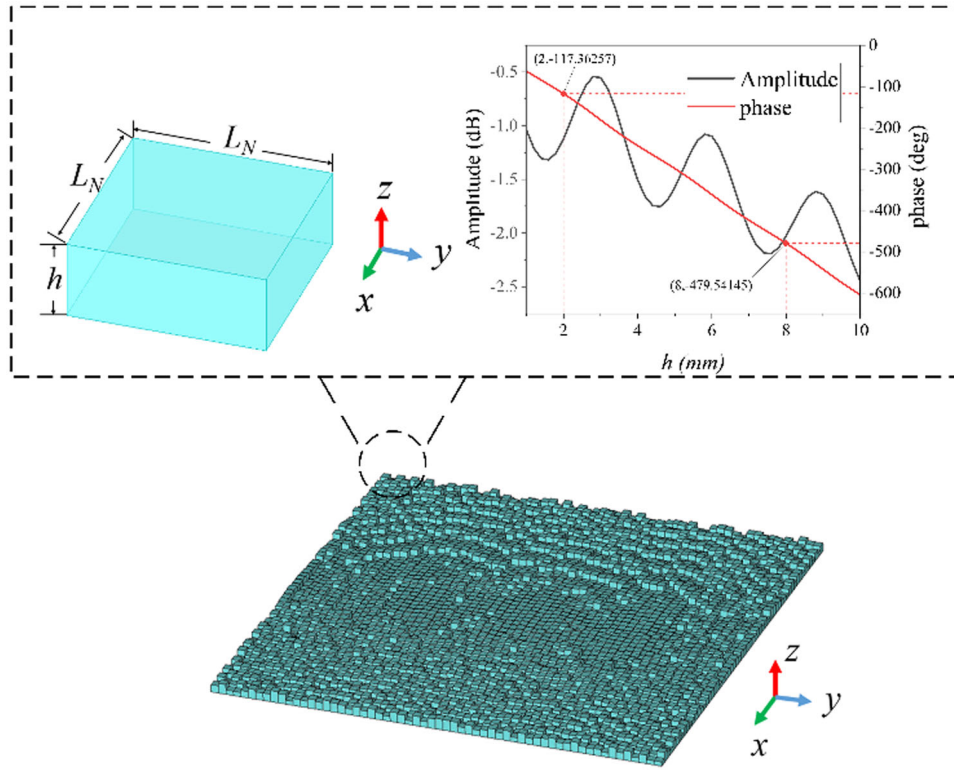
FIGURE 6 | Diffraction layer model, showing the geometric parameters and the relationship between amplitude and phase across the layer.

material VeroWhitePlus for 3D printing. The relative permittivity of the dielectric material $\varepsilon_r = 2.802$, the relative permeability $\mu_r = 1$, the loss tangent angle $\tan\delta = 0.0357$, and the simulation results of S_{21} at 30 GHz are shown in Figure 6. At $h = 2\,mm$, the corresponding cumulative phase shift is $-117.36°$, and the corresponding cumulative phase shift at $h = 8\,mm$ is $-479.53°$, and the difference is $-362.17°$. After calculation, the correlation is $|R| = 0.99991$, which meets the linearity requirement. Therefore, it can be considered that when $h = 2 \sim 8\,mm$ changes linearly, a complete 360° linear phase shift control can be achieved. In addition, the maximum amplitude of S_{21} is -0.5 dB, the minimum is -2.19 dB, and the energy loss is less than 40%.

Based on the square metamaterial unit structure, the hardware part of DNN imaging can be realized. The unit height h changes in the range of $2 \sim 8\,mm$, and the corresponding additional phase φ_i changes in the range of $0 \sim 360°$. The corresponding mapping relationship is

$$\boldsymbol{h} = \boldsymbol{\varphi} \cdot \frac{h_{\max} - h_{\min}}{2\pi} + h_{\min} \qquad (12)$$

Here $h_{\min} = 2\,mm$ is the uniform base height, which is also the zero phase reference surface, then $h_{\max} = 8\,mm$, $\boldsymbol{\varphi} = \begin{bmatrix} \varphi_{1,1} & \cdots & \varphi_{1,L_N} \\ \vdots & \ddots & \vdots \\ \varphi_{L_N,1} & \cdots & \varphi_{L_N,L_N} \end{bmatrix}$ is the hidden layer tensor matrix obtained by the DNN training imaging. According to the height matrix $\boldsymbol{h}$, the script is written to model the diffraction layer. The CST MICROWAVE STUDIO Suite 2020 is used for simulation solution. The simulation frequency is set to
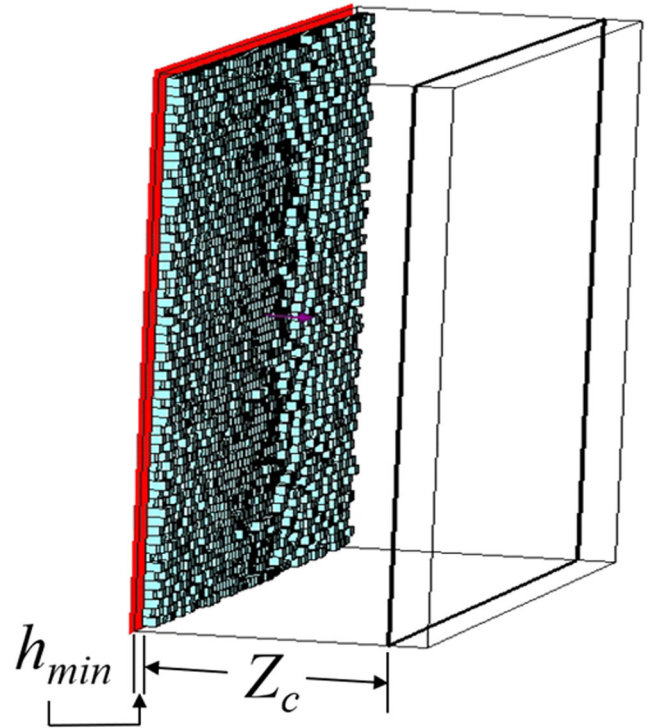

FIGURE 7 | Simulation imaging structure in CST.

30 GHz in the time domain solver. The plane wave excitation along the x-axis is added, and the open space boundary is set. The imaging plane is set to be 100 mm away from the zero-phase reference surface of the diffraction layer
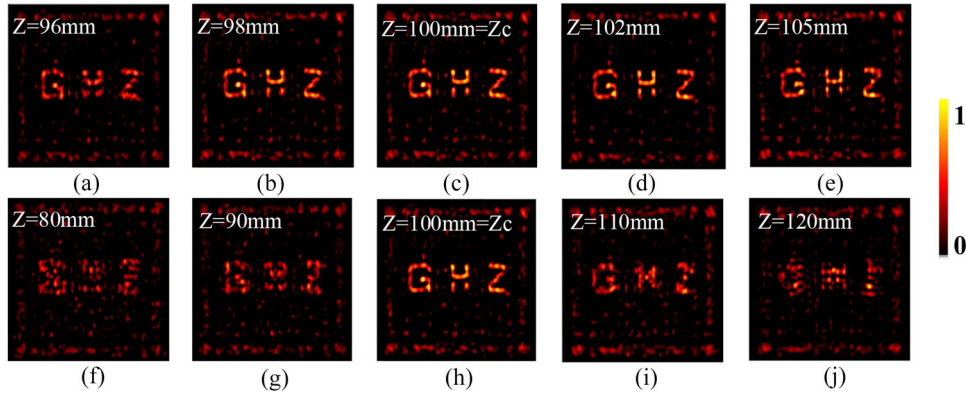
FIGURE 8 | (a–e) Simulation imaging results in a small range near the target plane. (f–j) Simulation results in a wide range near the imaging plane.
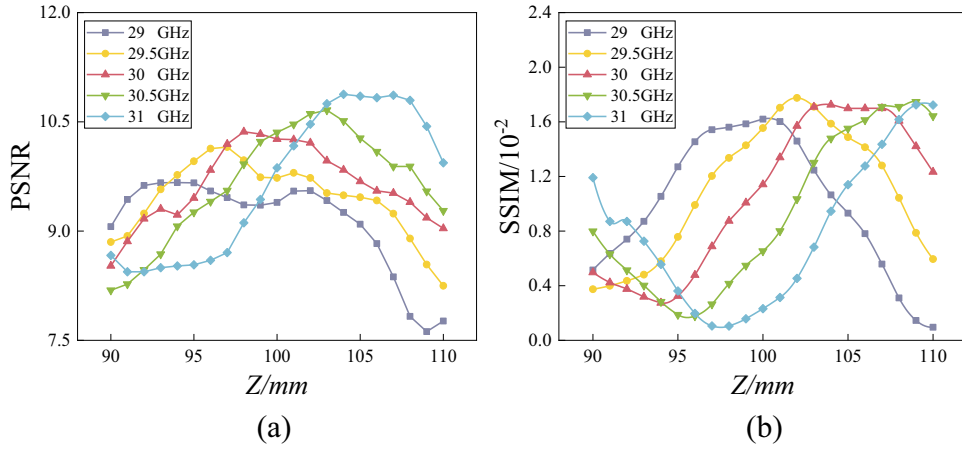

FIGURE 9 | (a) PSNR at 29-31 GHz and 90-110 mm. (b) SSIM in the same case.

(i.e. $z = 102\,mm$). The imaging structure is shown in Figure 7. The red area represents the plane wave illumination, and the heavy black square border represents the imaging plane. The diffraction theory mentioned in II. Methods regard the electric field and magnetic field as independent of each other, so the imaging plane measures the average value of the electric field intensity to represent the diffraction field: $U = |\bar{E}|$.

The simulation results are shown in Figure 8. After removing the substrate height, the electric field intensity ($\bar{E}$) distribution on different planes is taken out. For example, the imaging effect difference in the small range ($\pm 0.5\lambda_c$) from the target plane is not obvious in Figure 10a–e. And Figure 10f–j shows that the imaging effect is significantly different when it changes in a large scale range ($\pm 2\lambda_c$) comparable to the wavelength, indicating that the imaging is concentrated near the target plane and the focusing area is in a wavelength range. The simulation results preliminarily verify the feasibility of using DNN for microwave imaging.

To quantify the comparison, we use the structural similarity index (SSIM) to measure, and SSIM is defined as:
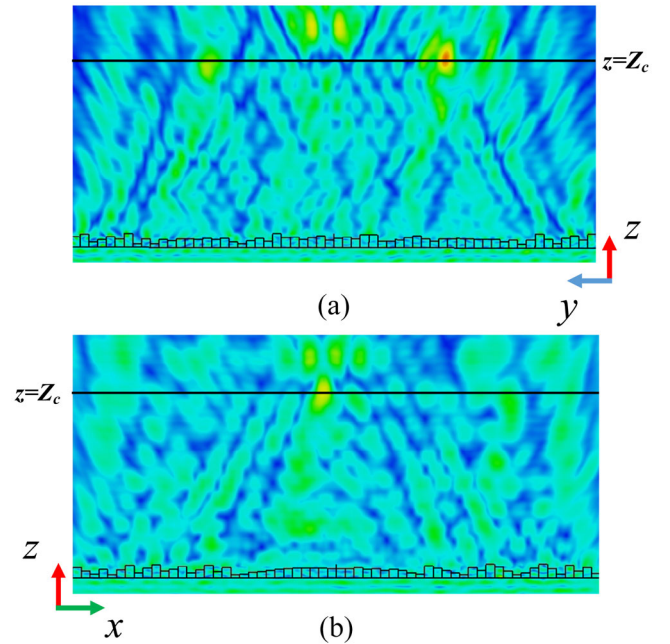

FIGURE 10 | (a) The E-field of YZ plane (X = 150 mm). (b) The E-field of XZ plane (Y = 150 mm).

$$SSIM(I_1, I_2) = l(I_1, I_2) \cdot c(I_1, I_2) \cdot s(I_1, I_2) = \frac{2\mu_1\mu_2}{\mu_1^2 + \mu_2^2}$$

$$\cdot \frac{2\sigma_1\sigma_2}{\sigma_1^2 + \sigma_2^2} \cdot \frac{\sigma_{1,2}^2}{\sigma_1\sigma_2} \tag{13}$$

where $l(I_1, I_2)$ is the luminance similarity, $c(I_1, I_2)$ is the contrast similarity, and $s(I_1, I_2)$ is the structure similarity. μ_1 and μ_2 are the average of I_1 and I_2. σ_1^2 and σ_2^2 are thevariances of I_1 and I_2. $\sigma_{1,2}^2$ is the covariance of I_1 and I_2. The SSIM is less than 1. The larger the SSIM is, the more similar the two images are.

The PSNR and SSIM index at different imaging planes at five frequency points are shown in Figure 9. There are good indicators at the preset frequency and plane. At the same time, the curve shows that the imaging has a certain spectral width, and the performance of the higher frequency band is better than

that of the lower frequency band, which should be due to the worse focusing performance of the low frequency wave.

Figure 10 shows the field distribution of the YZ plane and the XZ plane. The nonuniform diffraction layer on the surface adds a surface phase gradient to the outgoing electromagnetic wave, so that the electromagnetic wave beam is deflected and the energy is focused on the imaging plane. This principle can be explained by the generalized Snell's law. However, the calculation of the 3600 units of the 2D array and the DNN algorithm makes the image show more detailed details, which allows the letters "GHZ" to be displayed.

To demonstrate the technical advancements, we compare the traditional GS algorithm for solving hologram phase with our proposed approach. Following the GSW method outlined in Ref. [18], phase iteration was conducted 1000 times on the same
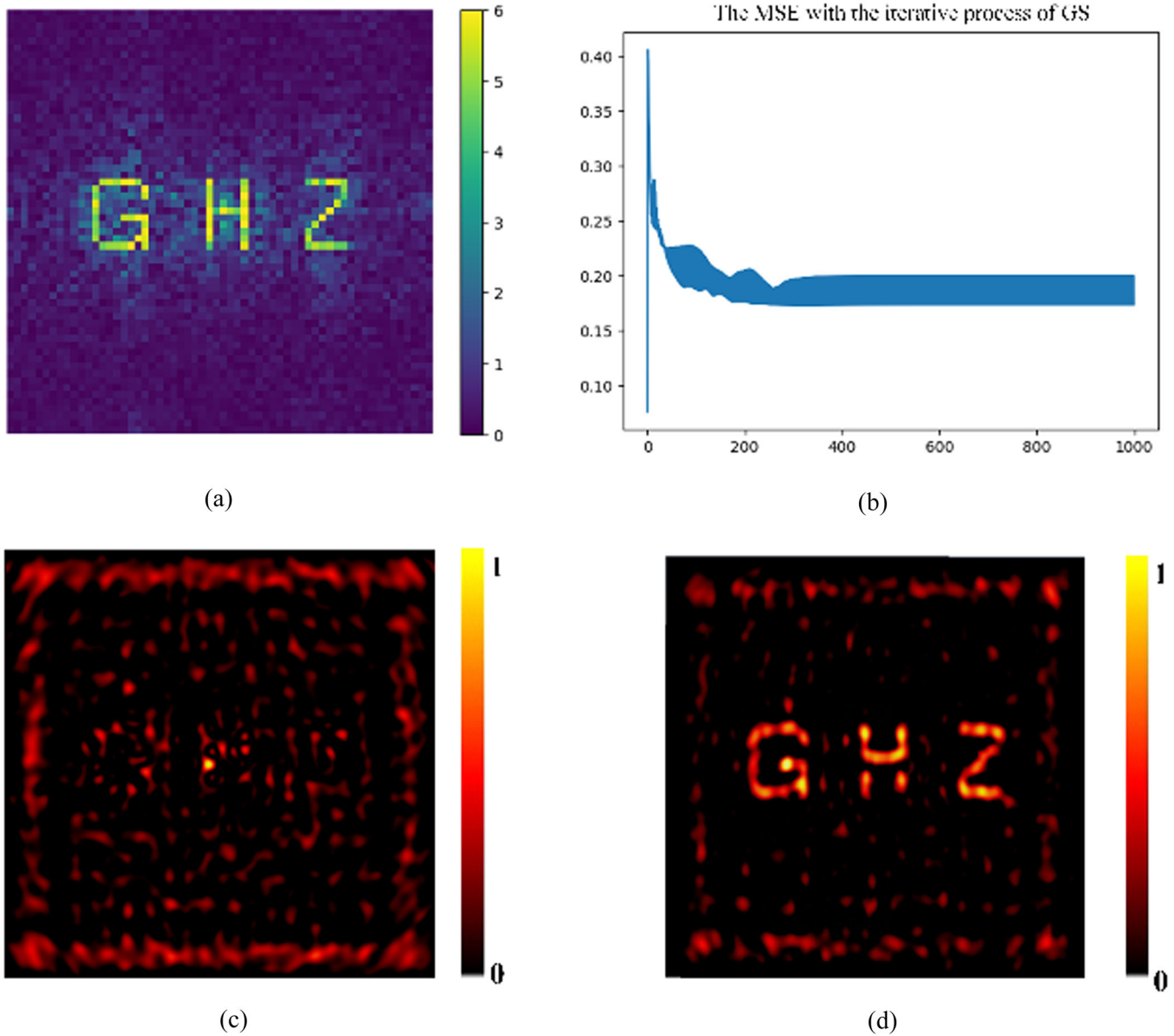

(a)

(b)

(c)

(d)

FIGURE 11 | Optimized imaging results obtained using the traditional GS algorithm. (a) shows the holographic image generated after 1000 iterations of phase adjustment. (b) illustrates the MSE variation during the iterative process, indicating a convergence to a stable phase solution. (c) presents the simulation results in CST, and (d) displays the field distribution calculated by the DNN for comparison.

TABLE 2 | Comparison of imaging quality metrics between DNN and GS algorithm.

	GS Algorithm	DNN
IE	0.2251	**0.6834**
PSNR	7.81 dB	**10.47 dB**
Time cost	22 m 50 s	**15 s**

computing device. The optimized imaging results obtained via the angular spectrum method are presented in Figure 11a. Figure 11b shows the MSE variation during the iterative process, indicating that the phase-solving process has reached a relatively stable convergence state. The simulation results in CST are displayed in Figure 11c, while the corresponding field strength distribution computed by the DNN is shown in Figure 11d. The quality of the holographic image was assessed using three metrics: imaging efficiency (IE), peak signal-to-noise ratio (PSNR), and time cost. The data are summarized in Table 2, illustrating that DNN imaging outperforms the GS algorithm in terms of holographic image quality and efficiency.

4 | Conclusion

In this Letter, holographic imaging is realized in microwave band based on DNN. A DNN model based on forward propagation of angular spectrum theory and FFT algorithm and stochastic gradient descent based on loss function is established. The parameter requirements of DNN are analyzed theoretically. Then, a training example is used to verify the ability of model training to optimize phase distribution, and parameter experiments are designed to analyze the influence of network parameters on training imaging. Then, the phase control ability of the square dielectric unit to the electromagnetic wave is analyzed and calculated, which is verified in the electromagnetic simulation software. The square dielectric unit is used as the periodic structure unit of the metamaterial. Based on the mapping relationship of the phase height, the metamaterial entity of the diffraction layer in the DNN is constructed, and the imaging ability is verified in the electromagnetic simulation software. It is believed that it will also have a very broad application prospect in more complex artificial intelligence scenarios and new generation of computing architecture.

References

1. M. Pastorino, *Microwave Imaging[M]* (John Wiley & Sons, 2010).

2. P. K. Koner, A. Harris, and E. Maturi, "A Physical Deterministic Inverse Method for Operational Satellite Remote Sensing: An Application for Sea Surfacetemperature Retrievals[J]," *IEEE Transactions on Geoscience and Remote Sensing* 53, no. 11 (2015): 5872–5888.

3. X. Song, R. Guo, M. Li, et al., "Study on a Joint Inversion Algorithm for Acoustic and Electromagnetic Data Based on Contrast Source Inversion Method and Cross-gradient Constraint[C]." *International Conference on Electromagnetics in Advanced Applications (ICEAA)* (IEEE, 2019). 2019, 0875–0878.

4. X. Wang, T. Qin, R. S. Witte, et al., "Computational Feasibility Study of Contrast-Enhanced Thermoacoustic Imaging for Breast Cancer Detection Using Realistic Numerical Breast Phantoms[J]," *IEEE Transactions on Microwave Theory and Techniques* 63, no. 5 (2015): 1489–1501.

5. X. Li, S. C. Hagness, B. D. Van Veen, et al., "Experimental Investigation of Microwave Imaging via Space-Time Beamforming for Breast Cancer Detection[C]," *Microwave Symposium Digest* 2003 (2003 IEEE MTT-S International. IEEE): 379–382.

6. A. Kozma and D. L. Kelly, "Spatial Filtering for Detection of Signals Submerged in Noise[J]," *Applied Optics* 4, no. 4 (1965): 387–392.

7. A. W. Lohmann and D. P. Paris, "Binary Fraunhofer Holograms, Generated by Computer," *Applied Optics* 6, no. 10 (1967): 1739–1748.

8. B. R. Brown and A. W. Lohmann, "Complex Spatial Filtering With Binary Masks," *Applied Optics* 5, no. 6 (1966): 967–969.

9. R. W. Gerchberg, "Super-Resolution Through Error Energy Reduction[J]," *Optica Acta: International Journal of Optics* 21, no. 9 (1974): 709–720.

10. D. Psaltis, D. Brady, X. G. Gu, and S. Lin, "Holography in Artificial Neural Networks," *Nature* 343, no. 6256 (1990): 325–330.

11. I. T. Rekanos, "Neural-Network-Based Inverse-Scattering Technique for Online Microwave Medical Imaging[J]," *IEEE Transactions on Magnetics* 38, no. 2 (2002): 1061–1064.

12. A. Kerhet, M. Raffetto, A. Boni, et al., "A SVM-Based Approach to Microwave Breast Cancer Detection[J]," *Engineering Applications of Artificial Intelligence* 19, no. 7 (2006): 807–818.

13. H. Sami, M. Sagheer, K. Riaz, et al., "Machine Learning-Based Approaches for Breast Cancer Detection in Microwave Imaging[C]," *IEEE USNC-URSI Radio Science Meeting (Joint with AP-S Symposium). IEEE* 2021 (2021): 72–73.

14. S. Wassila, M. Lotfi, and M. S. Mohammed, "Breast Cancer Detection Using the SVR Approach for Different Configurations of Microwave Imaging System[C]." *6th International Conference on Image and Signal Processing and their Applications (ISPA)* (IEEE, 2019). 2019, 1–5.

15. J. Xiao, Z. Liu, P. Zhao, et al., "Deep Learning Image Reconstruction Simulation for Electromagnetic Tomography[J]," *IEEE Sensors Journal* 18, no. 8 (2018): 3290–3298.

16. X. Lin, Y. Rivenson, N. T. Yardimci, et al., "All-Optical Machine Learning Using Diffractive Deep Neural Networks," *Science (New York, N.Y.)* 361, no. 6406 (2018): 1004–1008.

17. D. Liao, K. F. Chan, C. H. Chan, Q. Zhang, and H. Wang, "All-Optical Diffractive Neural Networked Terahertz Hologram," *Optics Letters* 45, no. 10 (2020): 2906–2909.

18. Z. Wang, X. Ding, K. Zhang, et al., "Huygens Metasurface Holograms With the Modulation of Focal Energy Distribution," *Advanced Optical Materials* 6, no. 12 (2018): 1800121.